ADVANCED MATERIALS TECHNOLOGIES
www.advmattechnol.de

Tailoring Pore Networks – Gas Diffusion Electrodes via Additive Manufacturing

*Nils Weber, John Linkhorst, Robert Keller, and Matthias Wessling**

Additive manufacturing (AM) is a promising alternative to conventional electrode production due to its high freedom of design, excellent reproducibility, and a manifold choice of metals serving as substrates or even electrocatalysts in various electrochemical reactions. Nonetheless, porous gas diffusion electrodes (GDEs) have not been fabricated by AM due to the required resolution of the pore network in the micron to submicron range. Herein, the single-step fabrication of GDEs via AM is demonstrated for the first time. Selective laser melting is used to control the porosity, the pore diameter, and the electrochemically active surface area of the generated pore network by engineering the laser hatching strategy. In this way, the electrocatalytic activity of the fabricated GDEs is tuned for CO_2 electroreduction. The CO_2 reduction reaction is amplified whilst the competing hydrogen evolution reaction is mitigated at high current densities of 100 mA cm^{-2}. The presented method is a step further towards the production of next-generation electrodes with tailored gas diffusion layers, thereby boosting electrode performance in a wide range of electrochemical applications.

1. Introduction

Against the background of global climate change, the defossilization and electrification of the chemical industry are gaining increasing importance.[1] Besides reducing the combustion of fossil fuels, which serve as energy carriers in the production of many platform chemicals, this also includes the transition from conventional chemical conversions to electrochemical routes. With suitable electrodes, electricity can be used to drive chemical reactions at mild temperatures and pressures.[2]

In recent years, great progress has been reported in various electrochemical applications using gas diffusion electrodes (GDEs) whenever both a liquid and a gaseous stream are involved in the desired process. Owing to the porous nature of a GDE, liquid and gaseous species meet at the so-called triple-phase boundary, thereby decreasing diffusion pathways and improving mass transport of the reactants.[3,4] On the anode side, GDEs have demonstrated good potential for the oxygen evolution reaction, which is an important counterpart to many cathodic half-reactions, such as the hydrogen evolution reaction (HER) and the CO_2 reduction reaction (CO_2RR).[5] On the cathode side, GDEs have shown promising results in the electroreduction of CO_2 and carbon monoxide (CO) to value-added products, such as formic acid, ethylene, methanol, and ethanol.[6–9] GDEs have also shown good potential for the production of hydrogen peroxide, which can be applied in the electrochemical degradation of organic pollutants in waste water.[10] Moreover, GDEs have been used as oxygen depolarized cathodes to reduce the energy demand in the chlor-alkali process.[11,12] Coupling electrocatalysis with biological components, GDEs have also been applied in microbial and enzymatic fuel cells and for microbial electrolysis.[13] Given the wide variety of different use cases, a GDE must fulfill certain requirements with regard to its chemical and physical properties.

In general, a GDE is built up of several functional layers all contributing to its final performance. A macroporous and electrically conductive support layer is usually followed by a microporous gas diffusion layer that is functionalized with a catalyst of choice.[4,14] The catalyst is usually added in a successive process step (e.g., slot-die coating or spray coating) and drives the desired electrochemical reaction. Apart from that, certain additives, such as polymers (PTFE) or ionomers (Nafion and Sustainion), have been reported as beneficial for catalytic performance and long-term stability.[15–17] As of today, most electrochemical reactor designs focus on planar arrangements. However, tubular geometries have gained attention due to advantages such as high surface-to-volume ratio, less sealing requirements, and high-pressure operation.[18–20] For CO_2 electroreduction, reports

N. Weber, J. Linkhorst, R. Keller, M. Wessling
Chemical Process Engineering AVT.CVT
RWTH Aachen University
Forckenbeckstraße 51, 52074 Aachen, Germany
E-mail: manuscripts.cvt@avt.rwth-aachen.de
M. Wessling
Research Group
DWI - Leibniz-Institute for Interactive Materials
Forckenbeckstraße 50, 52074 Aachen, Germany

The ORCID identification number(s) for the author(s) of this article can be found under https://doi.org/10.1002/admt.202300720

DOI: 10.1002/admt.202300720

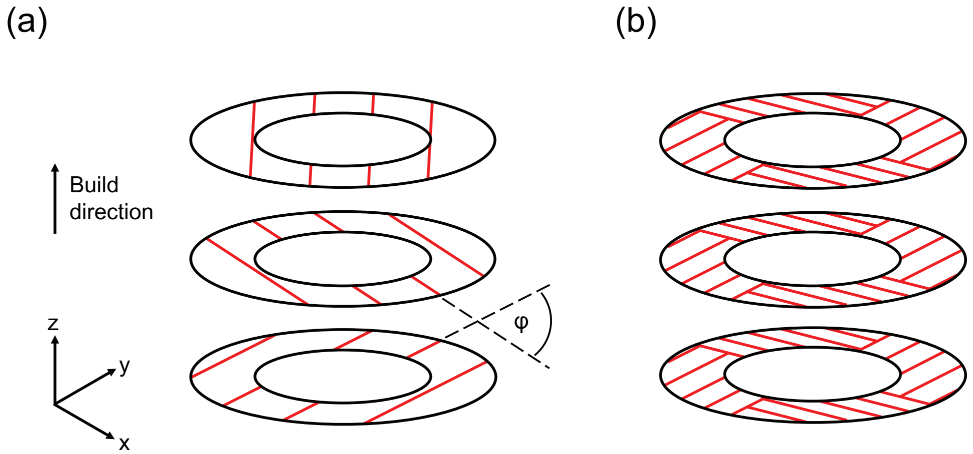

Figure 1. Laser hatching patterns applied for the additive manufacturing of GDEs. a) Stripes pattern with a rotation of $\varphi = 93°$ between every consecutive layer and b) chessboard pattern subdividing every layer into four equally sized quadrants.

on tubular geometries cover electrode fabrication via dry-wet spinning and subsequent sintering.[21–25] Even though progress has been made in the manufacturing, the production of GDEs remains a complex and time-consuming multi-step process.

Additive manufacturing (AM), however, offers a high freedom of design and has already demonstrated its potential for the production of porous electrodes and gas diffusion layers. AM has been used for the production of two-component (polymer/metal) gas diffusion layers,[26] all-metal liquid/gas diffusion meshes,[27] and flow-through electrodes.[28–31] Further work has focused on porous stainless steel structures through selective laser melting (SLM) and how the manufacturing parameters affect the porosity of the printed parts.[32–36] As shown in our recent work, SLM enables the production of porous flow-through electrodes via targeted control of the laser hatching strategy.[37,38] This results in a geometrically undefined porosity and high surface areas crucial for electrochemical conversions. However, to the best of our knowledge, there are no reports on 3D printed GDEs for electrochemical applications involving both a liquid and a gaseous phase.

In this study, we present the single-step fabrication of GDEs on a conventional laser powder bed fusion (LPBF) machine. We show that the energy density applied during the manufacturing process has a substantial impact on the resulting electrode porosity. By fine-tuning the manufacturing parameters, we are able to generate pores in the range from below 1 µm up to over 30 µm, thereby controlling the permeability of the GDEs and their electrochemically active surface area (ECSA). Eventually, we demonstrate their potential for CO_2 electroreduction at high current densities of 100 mA cm^{-2}. The control over the generated pore network allows for amplifying the CO_2RR and mitigating the competing HER.

2. Results and Discussion

2.1. Electrode Production and Physical Characterization

Two different laser hatching patterns, as depicted in **Figure 1**, were applied for the additive manufacturing of tubular GDEs. On the one hand, a parallel stripes pattern was used and the pattern was rotated by $\varphi = 93°$ every consecutive layer, as already described in our previous publication.[37] On the other hand, a chessboard pattern was used to investigate the effect of a directed, channel-like, pore network. Consequently, the cross section of the tubular electrode was divided into four quadrants of equal size and the laser scan lines were rotated by 90° between adjacent quadrants.[39]

In a first step, electrodes with different porosities were printed with the chessboard pattern by varying the energy density (cf. Equation (1)). **Figure 2** shows the porosities of thirteen electrodes

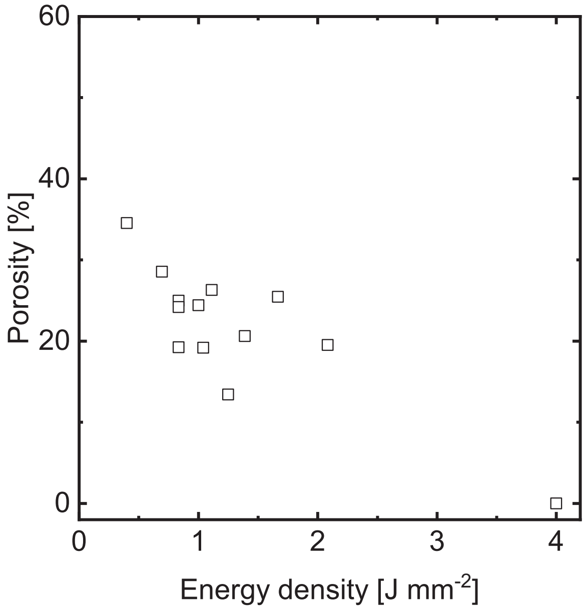

Figure 2. Porosity of GDEs as a function of the energy density applied during the SLM process (a layer thickness of 20 µm was used). In general, a decreasing energy density renders a more porous electrode up to a porosity of approximately 35%, at which a mechanically stable buildup becomes challenging.

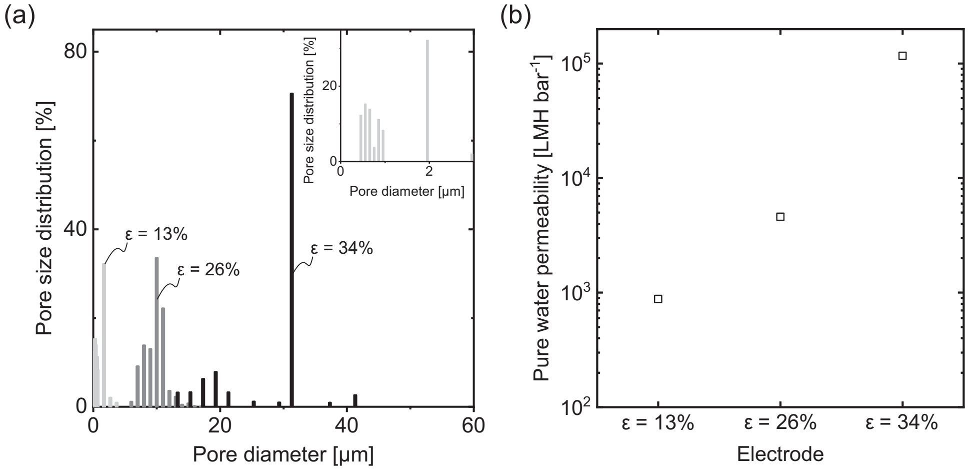

Figure 3. a) Pore size distribution of GDEs printed with a porosity of 13% (light grey), 26% (grey), and 34% (black), respectively. The latter was manufactured with the stripes pattern, whereas the chessboard pattern was used for the other two GDEs. The upper right corner shows a close-up of the pore diameter range between 0 and 3 µm. SLM allows for generating pores over a wide size range from over 30 down to 0.5 µm pore diameter. b) Pure water permeability measurements of the same GDEs reveal an increasing permeability with increasing porosity as a result of a greater void space within the porous wall of an electrode.

printed with a different set of applied laser power, hatching distance and scan speed, thereby altering the energy density. The layer thickness was kept constant at 20 µm. An energy density of 4 J mm^{-2} results in a full material electrode having no quantifiable porosity. Decreasing the energy density, however, leads to increased porosity. A porosity of up to 35% could be realized with an energy density of 0.4 J mm^{-2}. Further decrease in the energy density leads to insufficient melting of the copper powder and hence a mechanically stable buildup of an electrode is not possible. The results also demonstrate that one value of energy density can yield different porosities. Electrodes manufactured with an identical energy density of approximately 0.8 J mm^{-2} show different porosities as they were produced with a different set of applied laser power, hatching distance, and scan speed, respectively. Here, the scan speed was kept constant at 1200 mm s^{-1} for the three electrodes manufactured with 0.8 J mm^{-2} energy density. Among them, the most porous electrode (about 25% porosity) was manufactured with 80 W laser power and 80 µm hatching distance. The least porous electrode (about 19% porosity) was manufactured with 120 W laser power and 120 µm hatching distance. The electrode in between (about 24% porosity) was manufactured with 100 W laser power and 100 µm hatching distance. In this specific case, laser power is the dominant factor. Although an increase of the hatching distance might suggest a rising porosity, the electrodes become less porous as the elevated laser power leads to a more intense melting of the copper powder. Therefore, the energy density is a useful measure to estimate the resulting porosity in an initial assessment. However, for more accurate control, the complex interplay of the manufacturing parameters needs to be taken into account, as reported for the additive manufacturing of stainless steel.[34,36]

For detailed characterization of the pore network, the pore size distribution was investigated using a gas-liquid porometer. **Figure 3**a gives the pore size distribution of three electrodes manufactured with a porosity of 13%, 26%, and 34%, respectively. The results show that pore size can be controlled over several orders of magnitude using SLM. Similar to our previous report on stainless steel substrates,[37] we were able to produce electrodes with porosities of up to 26 and even 34% and pore diameters between 10 and 30 µm with copper. However, in this work, we were able to even decrease the pore diameter of the least porous electrode (13% porosity) down to 0.5 µm, pushing the boundaries toward the submicron and nanometer range. At the same time, all three electrodes are characterized by a narrow pore size distribution, which indicates a uniform nature of the pore network. To assess the permeability of the pore networks, pure water permeability measurements were performed with the same three electrodes. As pictured in Figure 3b, the pure water permeability of the least porous electrode is approximately 900 LMH bar^{-1}. It increases to about 5000 LMH bar^{-1} for the electrode with 26% porosity and further rises to over 100000 LMH bar^{-1} for the most porous electrode. The pure water permeabilities are thus in line with the measured porosities.

2.2. CO_2 Electroreduction

Three types of GDEs E1, E2 and E3 were manufactured using a chessboard pattern and a layer thickness of 20 µm, as listed in **Table 1**. Electrode E1 was produced with 13% porosity and a main pore diameter of 1 µm. Main pore diameter refers to the pore diameter with the highest share on the pores quantified in a porometer. Electrode E2 was printed with the same manufacturing parameters as electrode E1, only that the hatching distance was increased from 80 to 120 µm. This resulted in a higher porosity (24%) and larger main pore diameter (8 µm). Electrode E3 was manufactured with the same scan speed as electrodes E1 and E2, but the laser power was decreased to 80 W and the hatching distance was reduced to 60 µm. This yielded a similar porosity (26%) and pore size (10 µm) to electrode E2.

Figure 4 shows scanning electron microscopy (SEM) images of the cross-sectional areas of the three electrodes. As can be

Table 1. For CO_2 electroreduction experiments, three types of GDEs (E1, E2 and E3) were manufactured with different laser hatching strategies using a chessboard pattern and a layer thickness of 20 µm. P denotes the laser power, d is the hatching distance and v corresponds to the scan speed. Main pore diameter refers to the pore diameter with the highest share on the pores quantified in a porometer.

GDE	P [W]	d [µm]	v [mm s^{-1}]	Energy Density [J mm^{-2}]	Porosity [%]	Main Pore Diameter [µm]
E1	120	80	1200	1.25	13	1
E2	120	120	1200	0.83	24	8
E3	80	60	1200	1.11	26	10

seen from Figure 4a,d, electrode E1 has a pore network that looks dense with small voids in between. The applied chessboard pattern is barely discernible. This can be explained by the intense melting of the copper powder as a result of a comparably high laser power (120 W) and a narrow hatching distance (80 µm). Electrode E2, pictured in Figure 4b,e, is characterized by a channel-like structure and the chessboard pattern is clearly visible due to the wider hatching distance (120 µm). Figure 4c,f show electrode E3 that again has a distinct pore network different from electrodes E1 and E2. Here, the lower laser power (80 W) coupled with a more narrow hatching distance 60 µm) lead to a less intense melting of the copper powder. This creates an undirected pore network, even though electrode E3 was manufactured using a chessboard pattern. The SEM images match the results for the porosity and pore size distribution whilst giving a more complete image of the different pore networks.

Because copper is a well-known catalyst for electrochemical CO_2 conversion, CO_2 electroreduction experiments were carried out in an H-cell setup. As commonly reported for tubular electrodes, humidified CO_2 was forced from the lumen side through the pore network into the catholyte bulk.[22–25] The electrochemical setup is pictured in **Figure 5** and explained in detail in the Experimental Section.

Figure 6 shows the Faraday efficiencies for both gaseous and liquid products achieved with the three types of electrodes E1, E2, and E3 at a current density of 100 mA cm^{-2}. Using electrode E1, carbon monoxide (CO), formic acid (HCOOH), ethylene (C_2H_4) and methane (CH_4) could be synthesized, which are products commonly reported for CO_2 electroreduction on copper surfaces.[40–42] However, the hydrogen evolution reaction (HER) is predominant with a Faraday efficiency of over 80%.

On the one hand, this can be explained by the low electrode porosity of 13%, thereby yielding a comparably low surface area available for the CO_2RR. On the other hand, the triple-phase boundary is located close to the shell surface. **Figure 7**a shows the bubble formation on electrode E1 in deionized water when CO_2 is forced through the porous walls under no electrical current. As can be seen, the main pore diameter of 1 µm results in an almost complete coverage of the shell surface with CO_2. Thus, during CO_2 electroreduction a large part of the CO_2 is dissolved

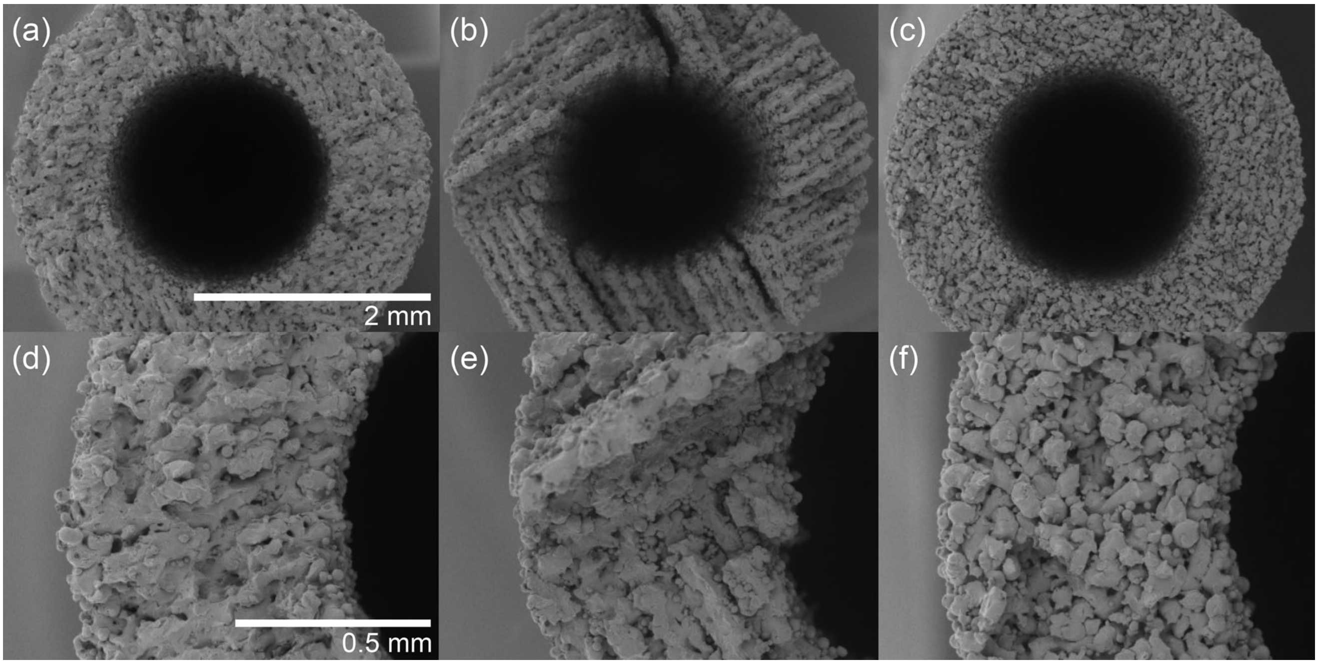

Figure 4. a) Cross-sectional view and d) close-up view of electrode E1. A comparably high laser power and narrow hatching distance lead to an intense melting of the copper particles and thus to a comparably low porosity and small pores. b) The cross sectional view and e) close-up view of electrode E2 reveal a directed and channel-like structure with a higher porosity and larger pores as a result of the increased hatching distance. c) The cross sectional view and f) close-up view of electrode E3 show that decreasing both the laser power and the hatching distance results in an undirected pore network with a similar porosity and pore size compared to electrode E2.

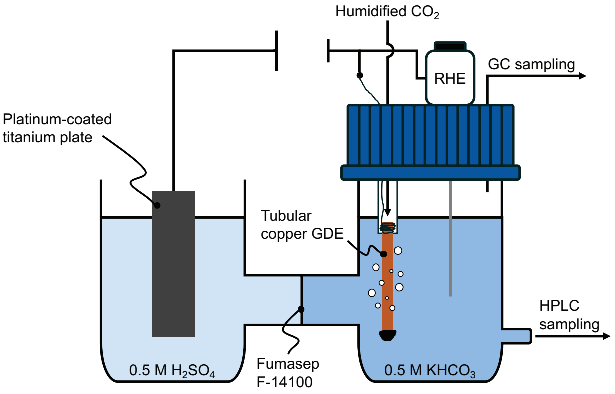

Figure 5. Electrochemical setup used for CO_2 electroreduction. The tubular copper GDE is glued with two-component epoxy adhesive at one end to force the CO_2 through the porous walls. The opposite end is wired to the electrical circuit and glued into a hose. Product analysis is carried out via GC and HPLC sampling.

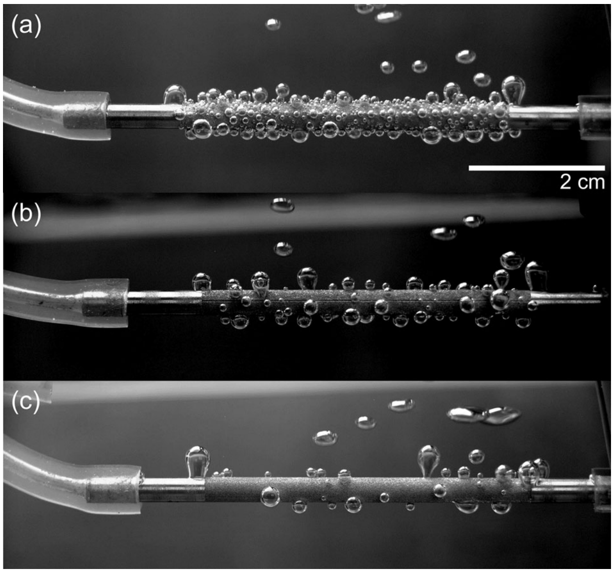

Figure 7. CO_2 bubble formation on electrodes E1, E2, and E3 in deionized water when no electrical current is applied. a) Electrode E1 with a main pore diameter of 1 µm is characterized by a high CO_2 coverage of the shell surface. b) On electrode E2, fewer and larger bubbles evolve owing to the larger main pore diameter of 8 µm. c) The effect is even more pronounced on electrode E3 with a main pore diameter of 10 µm.

in the electrolyte only at the electrode shell surface, which leads to a low amount of dissolved CO_2 in the vicinity of the catalyst, and hence the HER is predominant.

Using electrode E2, the same gaseous and liquid products can be observed. However, the percentage of products formed by the CO_2RR is higher compared to electrode E1, especially with regard to CO, HCOOH, and C_2H_4. This can be explained by the different nature of the pore network of electrode E2. Electrode E2 is characterized by both a higher porosity (24%) and a larger main pore diameter (8 µm), which leads to an increased ECSA available for the CO_2RR. By conducting cyclic voltammetry and plotting the current density over the applied scan rates, see **Figure 8**b, the double layer capacitance of electrode E2 was determined as 6.3 µF cm^{-2} whereas it is only 2.7 µF cm^{-2} for electrode E1. Details on the cyclic voltammograms can be found in the Supporting Information, see Figure S1 (Supporting Information). The higher double layer capacitance of electrode E2 suggests an ECSA more than twice as large as electrode E1. In this way, more reaction sites are available on the electrode surface for the CO_2RR. However, some of the channels of electrode E2 are potentially blocked by perpendicular channels of the adjacent quadrant within the chessboard pattern, as can be concluded from Figure 4b. Most likely, this leads to unexploited surface area within the pore network and the full potential of electrode E2 is not unleashed. Apart from the increased ECSA, the triple-phase boundary is located closer to the lumen of electrode E2 in comparison to E1 due to larger pores. As can be seen in Figure 7b, fewer and larger bubbles form on the shell surface. A larger fraction of the surface is in contact with the electrolyte, thereby paving the way for electrolyte to penetrate into the pore network. This in turn increases the amount of dissolved CO_2 in the pore network, which provides more CO_2 for electroreduction on the catalyst surface.

The amplified CO_2RR becomes even more pronounced on electrode E3. Even though having a similar porosity (26%) and main pore diameter (10 µm) as electrode E2, the formation of CO, HCOOH, and C_2H_4 is noticeably intensified on electrode E3. The undirected pore network provides a larger ECSA, as can be concluded from Figure 8b. The capacitance of electrode E3 amounts 12.4 µF cm^{-2}, which is more than four times the capacitance of electrode E1. To assess the wetting behavior of the GDEs in more detail, contact angle measurements were conducted with 0.5 M $KHCO_3$ right after depositing a droplet and 13 min later. Details can be found in the Supporting Information, see Figure S2 (Supporting Information). As is clear from our results, the wetting

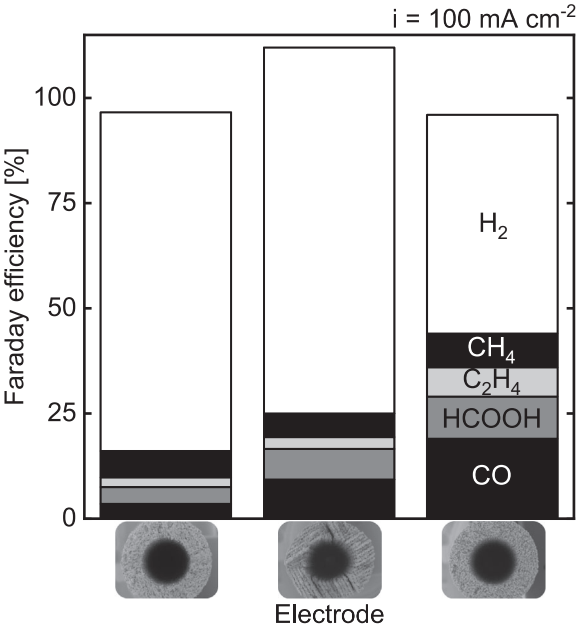

Figure 6. Faraday efficiencies of electrodes E1 (left), E2 (middle), and E3 (right) at a current density of 100 mA cm^{-2}. Changing the nature of the pore network has a direct impact on the CO_2RR, thereby mitigating the HER by approximately 30%.

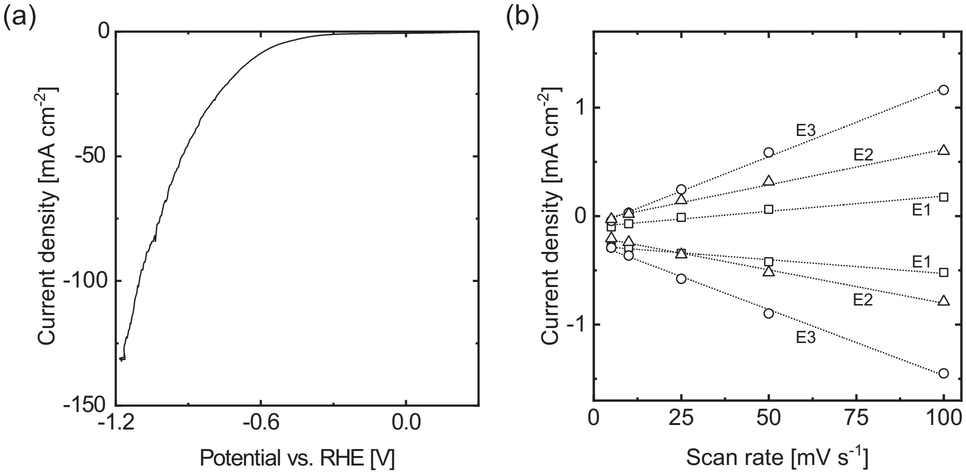

Figure 8. a) Linear sweep voltammogram of electrode E1 at a scan rate of 10 mV s^{-1} and CO_2 bubbling with 100 SmL min^{-1}. Compensation of the iR-drop was done with 80% compensation factor. b) Current density as a function of the applied scan rate for electrodes E1 (squares), E2 (triangles), and E3 (circles) including linear regression lines. The double layer capacitance, which corresponds to the slope, is lowest for electrode E1, followed by electrode E2 and electrode E3. Averaging the oxidative and reductive scans results in a capacitance of 2.7 µF cm^{-2} for E1, 6.3 µF cm^{-2} for E2 and 12.4 µF cm^{-2} for E3.

behavior appears similar for electrodes E1, E2, and E3 once a droplet is deposited onto the electrode surface. However, there is a time dependency in the penetration of the electrolyte into the pore network. Electrode E1 is least susceptible to flooding, whereas for both electrode E2 and E3 the droplet intrudes almost entirely after 13 min. This can be explained by the comparably small pores of electrode E1 (1 µm main pore diameter) as opposed to the larger pores of electrodes E2 and E3 (8 and 10 µm main pore diameter, respectively). These findings are in accordance with the observed bubble formation on the surface of the electrodes. According to Figure 7c, only few large bubbles form on the shell surface of electrode E3. We expect the triple-phase boundary to be located inside the porous electrode wall, where gaseous CO_2 is readily supplied from the lumen via diffusion. This in turn increases the amount of dissolved CO_2 in the vicinity of the catalyst. Consequently, the CO_2RR is amplified whilst the HER is mitigated by about 30% Faraday efficiency compared to electrode E1. Our results highlight the importance of controlling the local reaction environment.[43] A high advective transport of CO_2 toward the electrode does not guarantee high Faraday efficiencies for value-added products. Instead, the position of the triple-phase boundary needs to maximize the surface area between catalyst, gas, and liquid phase, which can be tailored by fine-tuning the manufacturing parameters.

3. Conclusion

The rising application of GDEs in manifold electrochemical conversions calls for alternative and well-controllable manufacturing methods. In this work, SLM was used for the first time to produce GDEs in a single step. By targeted modification of the laser hatching strategy, we could control the nature of the pore network. This is essential for contacting a liquid and a gaseous phase at the so-called triple-phase boundary that naturally forms inside a GDE.

We showed that fine-tuning the pore network requires consideration of the individual manufacturing parameters, such as laser hatching pattern, layer thickness, laser power, hatching distance, and scan speed. Mechanically stable electrodes with a porosity of up to 35% could be produced and physically characterized regarding their pore network. Pores could be generated over a wide size range from below 1 µm up to over 30 µm pore diameter. Moreover, pure water permeability measurements revealed an increasing permeability of more than 100000 LMH bar^{-1} with increasing electrode porosity due to the greater void space.

To demonstrate the potential of 3D printed GDEs, three types of GDEs were used for CO_2 electroreduction. The results indicate that the nature of the pore network has a substantial impact on the CO_2RR and hence the quantities of the formed products. By adjusting porosity, pore diameter, and the electrochemically active surface area of the pore network, we could control CO_2 bubble formation on the electrode surface and thus CO_2 surface coverage. This in turn affects the location of the triple-phase boundary essential for CO_2 electroreduction at industrially relevant current densities. We could amplify the CO_2RR and diminish the competing HER by about 30% at high current densities of 100 mA cm^{-2}.

As a next step, SLM could facilitate the production of planar GDEs that are used in many electrochemical applications, such as fuel cells, CO_2 electroreduction and chlor-alkali electrolysis. Moreover, composite porosity and composite pore size GDEs produced via SLM might open up new ways to control the position of the triple-phase boundary and enable fine-tuning of mass transfer, active surface area, and pressure drop. In this way, commonly reported electrode flooding could be tackled, thus improving long-term stability and extending the operation time of GDEs.

4. Experimental Section

Electrode Production: Print jobs were created in Magics 25.0.2.435 (Materialise NV) and processed with a SISMA build processor Version 6.1.00001.0 (Materialise NV). All electrodes were manufactured on an

LPBF machine (MySint100 PM, Sisma S.p.A.) equipped with a 200 W fiber laser. Copper powder (Infinite Powder Cu 01, Infinite Flex GmbH) with a medium particle diameter of 30 µm was used and sieved to a particle size < 60 µm prior to every print job. Electrodes were printed either with a stripes pattern, which was rotated by 93° every consecutive layer, or with a chessboard pattern, as visualized in Figure 1. Additionally, the following manufacturing parameters were altered: laser power, hatching distance, scan speed, and layer thickness. The energy density was calculated according to the following equation

$$ED = \frac{P}{d \cdot \nu} \tag{1}$$

with the energy density *ED*, laser power *P*, hatching distance *d* and scan speed *ν*. After printing, all electrodes were cleaned for 10 min in a ultrasonic bath in isopropanol to remove remaining powder. Electrodes were always stored under vacuum to prevent copper oxidation.

Physical Characterization: Physical characterization comprised an optical evaluation, porosity determination and the pore size distribution. For optical evaluation of the pore network, electrodes were broken in liquid nitrogen and SEM images were recorded using a tabletop microscope (TM3030plus, Hitachi). Porosity was determined according to

$$\epsilon = \frac{m}{\rho_{Cu} \cdot V} \tag{2}$$

with the porosity ϵ, electrode weight m, density of copper ρ_{Cu} (8960 kg m^{-3}) and the electrode volume *V*. To determine the pore size distribution, electrodes were immersed in a wetting fluid (Porefil, Porometer NV) and measured on a gas-liquid porometer (POROLUX 1000, Porometer NV).

Pure Water Permeability: Pure water permeability measurements were performed on a self-built test rig. One end of each electrode was glued with two-component epoxy adhesive (UHU Plus Sofortfest, UHU GmbH & Co. KG) and deionized water was forced through the porous walls of the electrodes at a constant pressure. Pure water permeability *PWP* was calculated from the permeate flow rate $\dot{V}$, the electrode shell surface *A* and the applied water pressure *p* according to the following equation

$$PWP = \frac{\dot{V}}{A \cdot p} \tag{3}$$

CO_2 Electroreduction: For CO_2 electroreduction, one end of each electrode was glued with two-component epoxy adhesive (UHU Plus Sofortfest, UHU GmbH & Co. KG) and the electrode was mounted as cathode into an H-cell setup, as pictured in Figure 5. On the anode side, a platinum-coated titanium plate was used as counter electrode. A reverse hydrogen electrode (Mini-HydroFlex RHE, Gaskatel GmbH) served as reference electrode. An aqueous solution (0.5 mol L^{-1}) of potassium bicarbonate (⩾99.7% purity, Carl Roth GmbH + Co. KG) served as catholyte, sulfuric acid (0.5 mol L^{-1}, Carl Roth GmbH + Co. KG) was used as anolyte and the electrolytes were separated by a cation exchange membrane (Fumasep F-14100, FUMATECH BWT GmbH). Before every experiment, the catholyte was saturated with CO_2 to ensure equal starting conditions. Electroreduction was performed in galvanostatic mode using a potentiostat (SP-150, BioLogic GmbH). To assess electrode performance at industrially relevant conditions, a current density of 100 mA cm^{-2} was applied, which was calculated using the shell surface of the electrodes. A linear sweep voltammogram of electrode E1 at a scan rate of 10 mV s^{-1} under CO_2 bubbling with 100 SmL min^{-1} is shown in Figure 8a. At 100 mA cm^{-2}, the potential is approximately −1.1 V versus RHE, which was comparable to copper nanoparticle-based conventional GDEs.[6] All electrodes were operated in flow-through mode, as reported earlier for tubular electrodes.[22–25] For this, humidified CO_2 was forced from the lumen side through the porous walls into the catholyte bulk at a flow rate of 100 SmL min^{-1}. An online gas chromatograph (Agilent 8860, Agilent Technologies Inc.) was used for product gas analysis. Offline analysis of the liquid products was carried out using a high performance liquid chromatograph (Agilent 1100 HPLC, Agilent Technologies Inc.).

Cyclic Voltammetry: To determine the double layer capacitance and to assess the electrochemically active surface area, cyclic voltammetry was conducted in an aqueous solution (0.5 mol L^{-1}) of potassium bicarbonate (⩾ 99.7% purity, Carl Roth GmbH + Co. KG). The same three electrode setup as for CO_2 electroreduction was used. Compensation of the iR drop was performed at 80% compensation factor. Before starting the experiment, each electrode was polarized at -0.15 V versus RHE for one hour. Subsequently, cyclic voltammetry was performed from −0.2 to −0.1 V versus RHE at 5 , 10, 25 , 50, $\sim$ and 100 mV s^{-1} scan rate. Every scan rate was cycled for five times and the last cycle was used for calculation of the double layer capacitance, where the oxidative and reductive current response were averaged.

Supporting Information

Supporting Information is available from the Wiley Online Library or from the author.

Acknowledgements

The authors wish to thank Alexander Limper, Tobias Harhues, Caroline Schmitz, Timo Linzenmeier, Justin Gottfried, Anselm Brodersen, Max Möntmann and Abdurrahman Öngün for their kind support. M.W. acknowledges DFG funding through the Gottfried Wilhelm Leibniz Award 2019 (WE 4678/12-1). N.W. and J.L. acknowledge funding by the Deutsche Forschungsgemeinschaft (DFG, German Research Foundation) under Germany's Excellence Strategy – Cluster of Excellence 2186 "The Fuel Science Center" – ID: 390919832. The SLM printer was funded under the same grant through the Junior Research Group CA2-JRG. This work was conducted in part at the "Competence Center for Industrial Electrochemistry ELECTRA", which is supported by the European Regional Development Fund (ERDF) and the Federal State of North Rhine-Westphalia (grant no. ERDF 0500077).

Open access funding enabled and organized by Projekt DEAL.

Conflict of Interest

The authors declare no conflict of interest.

Data Availability Statement

The data that support the findings of this study are available from the corresponding author upon reasonable request.

Keywords

CO_2 reduction, copper 3D printing, electrosynthesis, hollow fiber electrodes, selective laser melting, porosity

Received: May 8, 2023
Revised: July 27, 2023
Published online: September 3, 2023

[1] D. S. Mallapragada, Y. Dvorkin, M. A. Modestino, D. V. Esposito, W. A. Smith, B. M. Hodge, M. P. Harold, V. M. Donnelly, A. Nuz, C. Bloomquist, K. Baker, L. C. Grabow, Y. Yan, N. N. Rajput, R. L. Hartman, E. J. Biddinger, E. S. Aydil, A. D. Taylor, *Joule* **2023**, *7*, 23.

[2] Z. J. Schiffer, K. Manthiram, *Joule* **2017**, *1*, 10.
[3] T. Burdyny, W. A. Smith, *Energy Environ. Sci.* **2019**, *12*, 1442.
[4] D. Wakerley, S. Lamaison, J. Wicks, A. Clemens, J. Feaster, D. Corral, S. A. Jaffer, A. Sarkar, M. Fontecave, E. B. Duoss, S. Baker, E. H. Sargent, T. F. Jaramillo, C. Hahn, *Nat. Energy* **2022**, *7*, 130.
[5] S. Ogawa, K. Nakayama, M. Katayama, R. Ishikawa, Y. Ikuhara, M. Saito, T. Motohashi, *ACS Appl. Energy Mater.* **2022**, *5*, 15502.
[6] J. B. Vennekötter, R. Sengpiel, M. Wessling, *Chem. Eng. J.* **2019**, *364*, 89.
[7] Y. Y. Birdja, E. Pérez-Gallent, M. C. Figueiredo, A. J. Göttle, F. Calle-Vallejo, M. T. Koper, *Nat. Energy* **2019**, *4*, 732.
[8] H. Rabiee, L. Ge, X. Zhang, S. Hu, M. Li, Z. Yuan, *Energy Environ. Sci.* **2021**, *14*, 1959.
[9] M. Großeheide, D. Schaffeld, R. Keller, M. Wessling, *Electrochem. Commun.* **2023**, *150*, 0.
[10] J. Wang, C. Li, M. Rauf, H. Luo, X. Sun, Y. Jiang, *Sci. Total Environ.* **2021**, *759*, 143459.
[11] J. Kintrup, M. Millaruelo, V. Trieu, A. Bulan, E. S. Mojica, *Electrochem. Soc. Interface* **2017**, *26*, 73.
[12] K. Li, Q. Fan, H. Chuai, H. Liu, S. Zhang, X. Ma, *Trans. Tianjin Univ.* **2021**, *27*, 202.
[13] A. E. Horst, K. M. Mangold, D. Holtmann, *Biotechnol. Bioeng.* **2016**, *113*, 260.
[14] D. Higgins, C. Hahn, C. Xiang, T. F. Jaramillo, A. Z. Weber, *ACS Energy Lett.* **2019**, *4*, 317.
[15] E. W. Lees, B. A. Mowbray, D. A. Salvatore, G. L. Simpson, D. J. Dvorak, S. Ren, J. Chau, K. L. Milton, C. P. Berlinguette, *J. Mater. Chem. A* **2020**, *8*, 19493.
[16] C. Kim, J. C. Bui, X. Luo, J. K. Cooper, A. Kusoglu, A. Z. Weber, A. T. Bell, *Nat. Energy* **2022**, *7*, 116.
[17] U. O. Nwabara, A. D. Hernandez, D. A. Henckel, X. Chen, E. R. Cofell, M. P. De-Heer, S. Verma, A. A. Gewirth, P. J. Kenis, *ACS Appl. Energy Mater.* **2021**, *4*, 5175.
[18] K. Percin, O. Zoellner, D. Rall, M. Wessling, *ChemElectroChem* **2020**, *7*, 2665.
[19] G. Li, Y. Gou, J. Qiao, W. Sun, Z. Wang, K. Sun, *J. Power Sources* **2020**, *477*, 228693.
[20] A. Laube, A. Hofer, B. Sánchez Batalla, S. Ressel, A. Chica, S. Fischer, C. Weidlich, J. Bachmann, T. Struckmann, *Int. J. Hydrogen Energy* **2022**, *47*, 15943.
[21] R. Kas, K. K. Hummadi, R. Kortlever, P. De Wit, A. Milbrat, M. W. Luiten-Olieman, N. E. Benes, M. T. Koper, G. Mul, *Nat. Commun.* **2016**, *7*, 10748.
[22] D. Bell, D. Rall, M. Großeheide, L. Marx, L. Hülsdünker, M. Wessling, *Electrochem. Commun.* **2020**, *111*, 106645.
[23] I. Merino-Garcia, J. Albo, P. Krzywda, G. Mul, A. Irabien, *Catal. Today* **2020**, *346*, 34.
[24] A. Sustronk, N. Benes, G. Mul, *Electrochem. Sci. Adv.* **2021**, *3*, 2.
[25] S. Li, W. Chen, X. Dong, C. Zhu, A. Chen, Y. Song, G. Li, W. Wei, Y. Sun, *Nat. Commun.* **2022**, *13*, 1.
[26] A. Jayakumar, S. Singamneni, M. Ramos, A. M. Al-Jumaily, S. S. Pethaiah, *Materials* **2017**, *10*, 1.
[27] J. Mo, R. R. Dehoff, W. H. Peter, T. J. Toops, J. B. Green, F. Y. Zhang, *Int. J. Hydrogen Energy* **2016**, *41*, 3128.
[28] L. F. Arenas, C. Ponce de León, F. C. Walsh, *Electrochem. Commun.* **2017**, *77*, 133.
[29] V. A. Beck, A. N. Ivanovskaya, S. Chandrasekaran, J. B. Forien, S. E. Baker, E. B. Duoss, M. A. Worsley, *Proc. Natl. Acad. Sci. USA* **2021**, *118*, 1.
[30] L. F. Arenas, B. Miranda-Alcántara, N. Kaishubayeva, A. A. Abahussain, F. F. Rivera, C. Ponce de León, F. C. Walsh, *Trans. Inst. Met. Finish.* **2023**, *101*, 119.
[31] Y. Yu, S. Pei, J. Zhang, N. Ren, S. You, *Adv. Funct. Mater.* **2023**, *33*, 2214725.
[32] R. Li, J. Liu, Y. Shi, M. Du, Z. Xie, *J. Mater. Eng. Perform.* **2010**, *19*, 666.
[33] K. A. Ibrahim, B. Wu, N. P. Brandon, *Mater. Des.* **2016**, *106*, 51.
[34] T. Peng, C. Chen, *Int. J. Precis. Eng. Manuf. - Green Technol.* **2018**, *5*, 55.
[35] D. Jafari, W. W. Wits, T. H. Vaneker, A. G. Demir, B. Previtali, B. J. Geurts, I. Gibson, *Addit. Manuf.* **2020**, *35*, 101263.
[36] D. Xie, R. Dittmeyer, *Addit. Manuf.* **2021**, *47*, 102261.
[37] A. Limper, N. Weber, A. Brodersen, R. Keller, M. Wessling, J. Linkhorst, *Electrochem. Commun.* **2022**, *134*, 107176.
[38] F. Wiesner, A. Limper, C. Marth, A. Brodersen, J. Linkhorst, M. Wessling, *Adv. Eng. Mater.* **2023**, *25*, 1.
[39] D. Xie, B. Fränkle, C. Klahn, R. Dittmeyer, *Chem. Ing. Tech.* **2022**, *94*, 7.
[40] K. P. Kuhl, E. R. Cave, D. N. Abram, T. F. Jaramillo, *Energy Environ. Sci.* **2012**, *5*, 7050.
[41] R. Kortlever, J. Shen, K. J. P. Schouten, F. Calle-Vallejo, M. T. Koper, *J. Phys. Chem. Lett.* **2015**, *6*, 4073.
[42] J. B. Vennekötter, T. Scheuermann, R. Sengpiel, M. Wessling, *J. CO2 Util.* **2019**, *32*, 202.
[43] M. Heßelmann, B. C. Bräsel, R. G. Keller, M. Wessling, *Electrochem. Sci. Adv.* **2023**, *3*, 2100160.